Generation of a wingtip vortex pair using a pressure-side fin

Dominic Schröder, Thomas Leweke, Ralf Hörnschemeyer, Eike Stumpf

Generation of a wingtip vortex pair using a pressure-side fin

Dominic Schröder[a,*], Thomas Leweke[b], Ralf Hörnschemeyer[a], Eike Stumpf[a]

[a] *Institute of Aerospace Systems, RWTH Aachen University, 52062 Aachen, Germany*
[b] *IRPHE, CNRS, Aix-Marseille Université, Centrale Marseille, 13384 Marseille, France*

Abstract

We present results from a combined experimental and numerical investigation of the flow around a rectangular NACA 0012 wing, whose tip geometry is modified by the addition of a perpendicular fin. The purpose of this modification is to generate a system of two closely-spaced concentrated tip vortices, instead of the familiar single trailing vortex. Experiments were carried out in a water channel, where velocity measurements were made in the near wake of the wing using Stereoscopic Particle Image Velocimetry, in order to determine the characteristics of the tip vortex pair. Various configurations were tested by changing the position, dimensions and angle of attack of the fin. It was found that the fin could generate a strong and concentrated secondary vortex only when placed on the pressure side of the wing. Visualisations of surface streamlines using oil painting in a wind tunnel, as well as numerical simulations of the flow in the wingtip region, show that separation occurs with the fin on the suction side, even at low angles of attack. Both experiments and simulations were used to determine the influence of fin parameter variations on the tip vortex pair, with respect to its circulation ratio and separation distance. Whereas co-rotating vortex pairs of similar circulation could be generated easily, the fin's ability to produce counter-rotating secondary vortices is rather limited. The current results have relevance in the context of reducing the impact of concentrated tip vortices, which for rotor configurations can lead to strong blade-vortex interactions, causing fatigue and aerodynamic noise.

Keywords: Wingtip vortex, Vortex formation, Vortex pair

1. Introduction

The presence of vortices in flow fields containing finite-span lifting surfaces, such as aircraft wings, rotor blades and propellers, is a well-known phenomenon. As a direct physical consequence of the generated lift, the occurence of vortices trailing downstream of a finite wing is inevitable [1]. These wake vortices represent a possible threat to following aircraft, inducing a downwash and strong rolling moments, as well as large structural loads on the wing. Rossow [2], Gerz et al. [3] and Breitsamter [4] present detailed reviews of the research on fixed-wing aircraft wakes. In systems containing rotors, the blade tip vortices form a helical structure, due to the combination of free-stream velocity and rotational motion. Regarding helicopters in certain

*Corresponding author
Email address: schroeder@ilr.rwth-aachen.de (Dominic Schröder)

flight regimes, the interaction of a tip vortex with a following blade is responsible for unwanted noise and structural vibrations. Considering these negative effects of trailing vortices, numerous studies have been carried out to investigate the temporal and spatial evolution of these systems regarding their strength and possible mechanisms to accelerate their decay. Gerz et al. [3] divided the strategies to reduce the wake vortex hazard for fixed-wing aircraft into two categories. The first one approaches the problem by attempting to modify the vortex properties, e.g. by reducing the vorticity peak in the centre and increasing the core diameter (low-vorticity vortex design). One way to achieve this goal is to enhance the spreading of the vorticity field by means of modified wing control surfaces, as described e.g. by Coustols et al. [5]. In the 1970s, another approach to influence the strength of the wingtip vortex was proposed, the modification of the circulation distribution on the wing, since the spanwise loading has a direct impact on the vortex formation process. Rossow [6] presented a theoretical study deducing wing loadings resulting in a weaker tip vortex, and Corsiglia et al. [7] showed a reduction of the induced rolling moment by reshaping the spanwise loading.

Besides the formation of a "modified" vortex, a rapid decay presents the other approach to minimize wake danger. The enforcement of three-dimensional vortex instabilities leads to a quicker decay of the concentrated vortex structure. Jaquin et al. [8] describe the most eminent instabilities present in aircraft wakes. One way to trigger these instabilities is by interaction with other vortices. Leweke et al. [9] provide a detailed review of the dynamics and instabilities occurring in vortex pairs, covering both long- and short-wavelength instabilities. An enhancement of these phenomena can be achieved by either active or passive devices. Crouch et al. [10] presented a system of active control surfaces, e.g. ailerons and flaperons. Active Gurney flaps have been studied by Greenblatt et al. [11]. Passive elements, such as spoilers and fins, can also be used to modify the wake vortex. A highly turbulent flow zone is created by means of spoiler elements; it influences the roll-up and merging processes, resulting in a reduction of axial peak velocity and viscous core diameter [4]. The impact of a fin mounted on the wing, producing a secondary vortex for wake alleviation, was first investigated by Rossow [12]. An increased dispersion of the wake caused by the vortex injection was shown theoretically and verified experimentally. Özger et al. [13] presented a similar study, observing a remarkable effect of the injected fin vortex on the wake. However, a detailed analysis concerning the initial vortex properties as a function of the parameters defining the fin geometry was not provided. The knowledge of the initial vortex characteristics would enable a better prediction of the subsequent vortex interactions and the potential for wake alleviation.

In systems consisting of rotating blades, e.g. helicopter rotors or wind turbines, wake alleviation has been an active research topic over the past decades. The reduction or modification of blade-vortex interactions (BVI) as sources of unwanted noise and high structural loads has been of particular interest. Widnall [14] provided a theoretical model for the radiated sound level caused by BVI due to fluctuating lift characteristics. Schmitz & Yu [15] deduced the vortex core diameter as a decisive parameter for noise emission. Concepts for noise reduction based on a simplified model for BVI were provided by Hardin & Lamkin [16]. Comparable to the fixed wing, Yu [17] divides BVI reduction methods into active and passive systems. Active systems comprise concepts using higher-harmonic pitch control (HHC) and individual blade control (IBC) and showed promising results in terms of noise and vibration reduction [17, 18]. The passive concept targets an optimised blade geometry, especially in the tip region, in order to influence the vortex formation and vortex characteristics after the completed roll-up. Various concepts for blade tip geometries and their influence on the vortices have been investigated, aiming at splitting or diffusing the tip vortex [19]. Yu [17], Brentner & Farassat [20] and Brocklehurst & Barakos

[19] give detailed reviews on a variety of tip shapes investigated by experimental and numerical methods. The geometry proposed by Brocklehurst & Pike [21] leads to the formation of two distinct vortices instead of a single one. Splitting the vortices results in a noticeable reduction of BVI noise emissions, implying a modification of the vortex structure before it encounters the following blade. An explanation for this phenomenon may be found in the interaction process between the two distinct helical vortices, which can involve three-dimensional instabilities, leading to the eventual merging into a single vortex. Similar to straight vortices, Leweke et al. [22] divide the instability mechanisms for helical vortices into two groups, according to the resulting effects. The fist mechanism causes displacements of the whole vortex, with minimal effects on the internal core structure. These perturbations are described as long-wavelength instabilities, since their scale is large compared to the vortex core diameter. Theoretical and experimental studies regarding long-wavelength instabilities in helical vortices can be found in Refs. [23–25]. The other type of instabilities, referred to as short-wavelength instabilities, arises inside the vortex core, with perturbation wavelengths of the order of the core diameter. An analysis by Moore & Saffman [26] deduced the resonance of Kelvin modes by virtue of an external strain field as the origin of the instability. A review of this mechanism, known as elliptic instability since the base flow streamlines are ellipses, is given by Kerswell [27]. Blanco-Rodríguez & Le Dizès [28] demonstrated that curvature and torsion existing in helical vortex systems act as further sources for elliptic instabilities. An additional short-wavelength instability appears in helical vortex systems, the curvature instability. An analysis of this phenomenon was performed by Fukumoto & Hattori [29] for a vortex ring and extended to helical vortex systems in Refs. [30, 31].

In the present study, we focus on the concept of creating two distinct vortices at the tip of a fixed wing. Following an earlier study by Buffo et al. [32], we use the simple geometry of a rectangular wing and propose a method of generating a secondary vortex by adding a perpendicular fin on one side of the wing near the tip. Water channel and wind tunnel experiments, together with numerical simulations, are used to investigate the initial formation of the vortex system for this new wingtip geometry, and to determine the relation between the fin parameters (size, position, orientation) and the properties of the resulting vortex pair. In §2 below, details about the experimental methods and numerical simulations are given. The results are presented in §3, focussing on the qualitative effect of the fin in various positions and the conditions that produce a pair of tip vortices with similar circulation, which represents a favourable configuration for merging processes. Concluding remarks are given in §4.

2. Experimental and numerical methods

2.1. Experimental set-ups

The flow around the novel wingtip geometry was studied experimentally in two facilities located at the Institute of Aero-space Systems. The first is a recirculating water channel, with a closed test section of dimensions 100 cm (length) × 54 cm (width) × 54 cm (height) and a free-stream velocity range up to $U = 4$ m/s. The inflow velocity field within the test section has a turbulence level of ∼1.5% and is uniform to within less than 2% outside the wall boundary layers. The wing model was mounted vertically on the ceiling of the test section. A motorised crossbeam and rotation axis allowed for adjusting its spatial position and angle of attack (α). The majority of experimental results were obtained in this setup. In addition, oil painting visualisations of surface streamlines were made in a low-speed open-section wind tunnel, using the same wing model (see below).

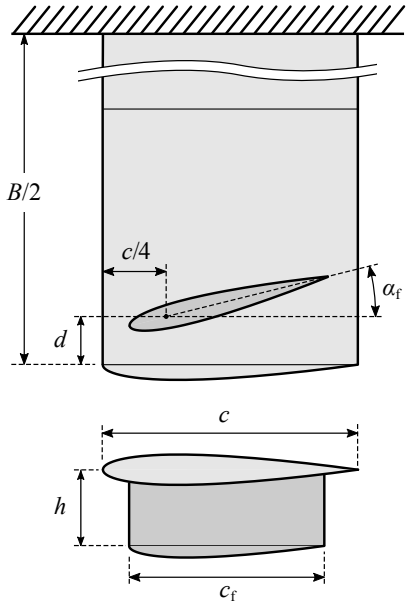

Fig. 1. Schematic side and end views of the wingtip geometry equipped with a fin.

The model itself consists of a rectangular half-wing of semi-span $B/2 = 29$ cm and chord $c = 10$ cm, giving a nominal aspect ratio $B/c = 5.8$. The cross-section has a NACA 0012 profile, and the wingtip is rounded with a body-of-revolution cap. The main wing body is manufactured from anodised aluminium. The tip geometry is interchangeable, it is attached using magnets and dowel pins to guarantee shape accuracy. In order to generate a secondary vortex, the wingtip was modified by adding a perpendicular fin located either on the suction or the pressure side. The fin geometry with its various parameters is shown schematically in Fig. 1. Like the main wing, it has a NACA 0012 cross-section and a rounded tip. Its chord is $c_\mathrm{f} = 8$ cm $= 0.8\,c$ for all cases investigated in this study. Its position (d), height (h) and angle of attack (α_f) were varied, in order to explore the effect on the trailing vortex system. The various tip configurations tested were manufactured by rapid prototyping (3D printing). The blockage ratio of the model within the water tunnel for the highest investigated angle of attack ($\alpha = 12°$) was 2.3%.

The Reynolds number based on the chord was kept constant at $\mathrm{Re} = Uc/\nu = 100,000$ (ν: kinematic viscosity) in all experiments. This was achieved by adjusting the free-stream velocity as function of the temperature-dependent viscosity of the fluid, i.e. in the range $U = 98$–102 cm/s for the water channel measurements.

2.2. Velocity measurements

The properties of the tip vortex system were determined from measurements of the velocity field in various downstream cross-sections of the flow. These fields were obtained in the water channel by Stereoscopic Particle Image Velocimetry (SPIV), which gives access to the three velocity components in a two-dimensional field of view. The lower and side walls of the test section are made of glass, allowing for the necessary optical access. Fig. 2 presents a schematic view of the measurement setup and the general coordinate system. The flow was seeded with

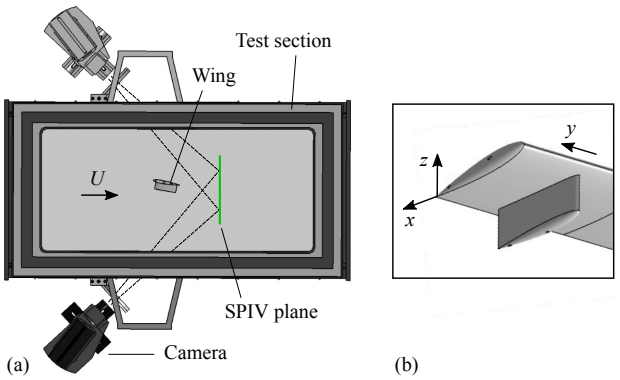

Fig. 2. (a) Experimental setup for SPIV measurements in the water channel (view from below). (b) Sketch defining the coordinate system.

cubic polyamide particles of mean diameter 50 µm and density 1.016 g cm^{-3} ensuring a good tracking of the fluid motion. The measurement plane was illuminated from below by a double-pulsed laser (Quantel Twins Ultra), with a pulse energy of 120 mJ, operating at an effective wavelength of 532 nm. The optics mounted in front of the laser provided a light sheet of 2–3 mm thickness, minimising the detection probability of unwanted particles located outside measurement plane. Particle images were recorded by two CCD cameras (PCO.2000) with a resolution of 2048 × 2048 pixles, placed on each side of the test section. The cameras were oriented at an angle of approximately 30°, matching the recommendation of Lawson & Wu [33] to minimise measurement errors in both the in-plane and out-of-plane velocity reconstruction. Adapters fulfilling the Scheimpflug criterion and water-filled prisms, as suggested by Prasad and Jensen [34], were used to minimise the aberrations due to the change of the optical medium. Two objectives with a focal length of 85 mm and f-number equal to 11 were used to record a 10 cm × 12 cm field of view. To avoid peak-locking errors, the particle diameter on the recorded images were set to approximately 3 pixels by adjusting the focal distance [35].

Calibration, image acquisition, synchronisation of light source and cameras, as well as image processing, were performed using the DaVis 8.4 software developed by LaVision. Calibration was achieved with a dual-plane calibration plate with circular markers (LaVision); the calculated calibration coefficients were within the satisfactory range. It was possible to use a single calibrated plane for all measurements, since the wing model could be traversed in the downstream direction. The double-frame/single-pulse technique was used for image acquisition. For each case, 350 images were recorded at a frequency of 3 Hz. A delay time of 380 µs between two subsequent images resulted in a satisfactory pixel shift and an acceptable loss-of-pairs. The subsequent stereo cross-correlation was a two-stage process, using first an interrogation window size of 64 × 64 pixels with an overlap of 50%, and then a smaller size of 32 × 32 pixels with an overlap of 75%, resulting in a final spatial resolution of 10–12 vectors within the vortex core radius. For both window sizes, 4 calculation passes were carried out. Further data analysis, including vortex identification, the calculation of vortex properties and statistical post-processing, were conducted with in-house Matlab routines.

A first survey was carried out with measurements in 4 planes at equidistant downstream positions (x/c =1–4) behind the trailing edge of the wing. In a second campaign, a reduced number of configurations was investigated in more detail, with an improved field of view and an

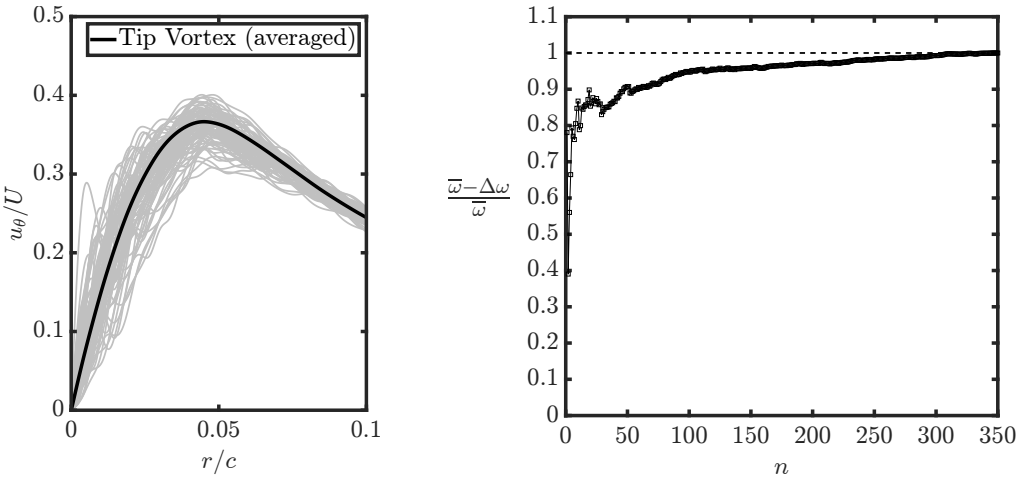

Fig. 3. (a) Instantaneous swirl velocity profiles of the tip vortex; the black line represents the profile obtained from the averaged velocity field. (b) Convergence ratio of the streamwise vorticity component ω at a point within the tip vortex core.

additional plane at $x/c = 6$.

2.2.1. Uncertainty analysis

The determination of vortex parameters is influenced by a variety of effects. Detecting the core centers is usually done by localising the maximum of a suitable flow field operator within the velocity field. This method requires valid information about the flow characteristics close to the core regions. However, due to the large centrifugal forces, the regions close to the vortex center are often affected by a lack of seeding particles, causing data voids that represent a drawback for tracer-based measurements of vortices, especially in wind tunnels. Water tunnels, in contrast, provide suitable conditions for the analysis of vortex-dominated flows for comparable Reynolds numbers, due to the reduced tangential velocities in the core regions. All measurements presented in this study exhibit a sufficient seeding density within the vortex cores, allowing the detection of the centers without the need of special filter techniques, e.g. the one proposed by van der Wall & Richard [36]. Another aspect which has to be considered is vortex wandering, see e.g. [37]. These irregular motion of the vortices between the recorded frames can cause a biased averaged swirl velocity profile, which affects the determination of the core radii and velocity peaks. Wandering is usually addressed by techniques such as conditional averaging [36], where the individual vortex centers are aligned before the averaging process. However, this technique is not feasible for our data, since two individual vortices are present within the flow field which both move separately. To identify the effect of wandering within this study, the instantaneous swirl velocity profiles are compared with the profile obtained from the averaged velocity field, an example is given in Fig. 3a) (The corresponding averaged vorticity contourplot of the example is shown in Fig. 10a, the profiles are obtained for the tip vortex). The calculation procedure of the swirl profiles and the center detection method is described in 3.1. The result shows a good agreement between the averaged and the instantaneous profiles with regard to the maximum value and the distance to the center. Deviations of the individual center positions compared to the average are found to be smaller than 1% of the wing chord, in accordance with the findings of

Devenport et al. [37]. Based on the analysis, the error within the core radius detection is estimated to lie in the range of 5-10%. To evaluate the uncertainty of the determined circulation values, the convergence of the streamwise vorticity component within an exemplary vortex core is shown in Fig. 3(b). Despite the expected high fluctuations within the core region, the vorticity converges to within well below 1% for less than 200 frames. The analysis of the instantaneous circulation values yields an uncertainty for the averaged value of 7-10%.

2.3. Visualisations

A closed-circuit low-speed wind tunnel with an open test section and a nozzle diameter of 1.5 m was used for surface streamline visualisations with the oil-painting method. The wing model with a fluorescent coating was positioned at the bottom of the open test section, with the tip pointing upwards. Two high-resolution cameras of 2048×2048 pixel resolution were used to capture the streamline formation and final steady-state condition. One camera covered a side view of the wing, recording the suction or the pressure side, depending on the fin position. The other camera was mounted above the model, with a field of view capturing the wingtip region and the outer side of the fin. All visualisations were performed at a Reynolds number of $\mathrm{Re} = 100,000$.

Only selected configurations, chosen on the basis of previous SPIV results, were tested. Particular attention was paid to the differences in flow behaviour when the fin was positioned on either the suction or the pressure side.

2.4. Numerical methods

The numerical simulations in the present study were carried out using the TAU code of DLR [38]. This code is an unstructured finite-volume solver for the compressible Reynolds-averaged Navier-Stokes (RANS) equations. Central discretisation schemes are used to compute the spatial derivatives in the RANS equations. To formally achieve second-order accuracy, an artificial matrix dissipation is applied [39]. The turbulence equations are discretised by a simplified Roe upwind scheme with second-order reconstruction from limited gradients. An implicit lower-upper symmetric Gauss-Seidel (LU-SGS) scheme with a three-step multigrid acceleration is applied to the RANS equations for the integration in pseudo-time. The turbulence equations are integrated on the finest grid levels only. Turbulence modelling is done with the SSG/LRR-ω Reynolds stress model [40], which directly builds on the modelled transport equations for the Reynolds stress tensor. Braun et al. [41] showed that this model provides good agreement with experimental data when simulating vortices and their formation process. The model is here improved with a recent modification to increase numerical robustness. A transformation of the length-scale equation allows an accelerated convergence even in regions with the finest mesh [42]. The dimensions of the computational domain are: $50c$ in the streamwise direction x, $20c$ in the spanwise direction y and $40c$ in the "vertical" direction z. No-slip boundary conditions are applied at the wing surfaces. The outer surfaces of the computational domain are implemented with far-field conditions, except for the one containing the wing root, where a symmetry condition is applied. The wing is centered on this symmetry plane.

The hybrid computational grid, consisting of prisms, hexahedrons and structured regions, was generated using the CENTAUR software. 55 structured prismatic layers are utilised in the direction normal to the wing and fin surfaces, in order to resolve the boundary layer region. The thickness of the first prism layer is chosen so that the normalised distance between the surface and the first node is less than unity in the entire domain, which guarantees the resolution of the viscous sublayer everywhere. Structured hexahedron blocks are used in regions where the vortex

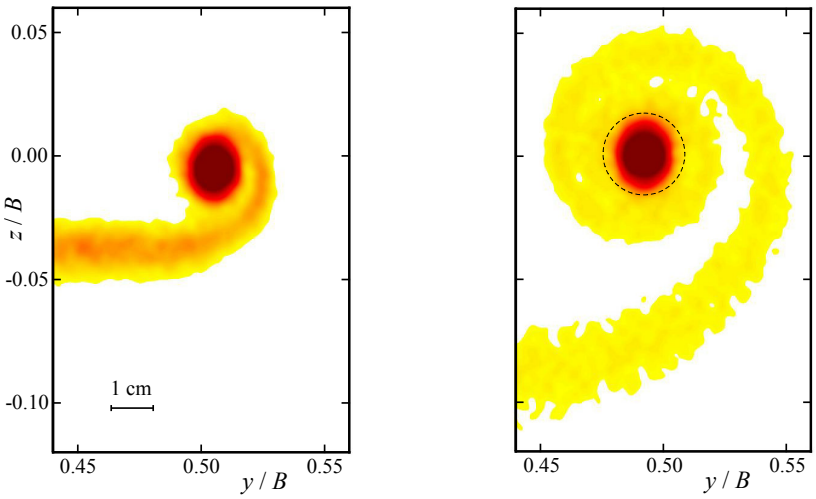

Fig. 4. Streamwise vorticity distribution at two downstream positions behind the bare wing at $\alpha = 10°$. The dashed circle in (b) has a diameter of $0.2c$.

formation process occurs, in order to resolve the rolled-up vortices with sufficient accuracy and minimise numerical dissipation. A grid step of $10^{-3}c$ is obtained in the structured regions, providing a resolution which is an order of magnitude higher than the one recommended by Dacles-Mariani et al. [43]. The grids of all investigated cases have approximately 26 million points. In order to allow comparability to the experimental measurements, the chord-based Reynolds number for all numerical calculations was set to the same value as in the experiments: Re = 100, 000.

3. Results and discussion

3.1. Tip vortex of the bare wing

In this study, the reference configuration (without fin) consists of a rectangular wing of aspect ratio $B/c = 5.8$, having a symmetric NACA 0012 cross-section profile and rounded tips. Previous experimental studies [44, 45] and numerical simulations [46, 47] of this geometry have shown that it generates a single concentrated tip vortex, whose strongly rotating core becomes axisymmetric and almost laminar within about one chord length behind the trailing edge of the wing. Fig. 4 shows examples of streamwise vorticity distributions obtained in the present experiments from SPIV measurements at two downstream positions. At $x/c = 1$ a high-vorticity vortex core is formed, connected to the low-vorticity vortex sheet shed behind the entire span of the wing. This sheet continues to roll up around the core as it moves downstream.

The vortex structure can be characterised by swirl velocity and circulation profiles. These were obtained by first transforming the velocity components in the cross-sectional y-z plane to a polar coordinate system r-θ around the vortex centre, which is determined with the λ_2-method proposed by Jeong and Hussain [48]. The resulting azimuthal velocity u_θ is then averaged on circles of radius r, and integrated along these circles for the circulation. The results for the field measured at $x/c = 6$ (Fig. 4b) are presented in Fig. 5 for angles of attack ranging between 4° and 12°. The circulation is normalised by the theoretical value $\Gamma_0 = \pi\alpha Uc$ for a thin airfoil in

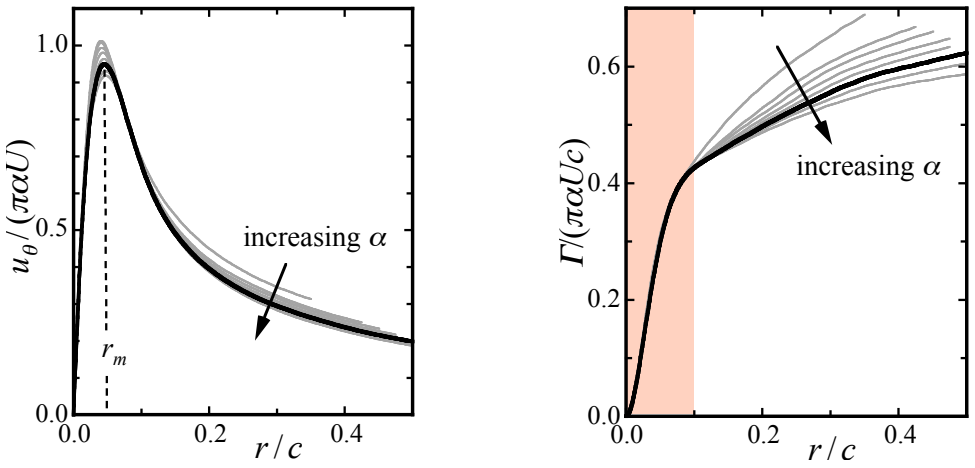

Fig. 5. Radial velocity and circulation profiles (azimuthal averages) of the tip vortex at $x/c = 6$, for α in the range 4°–12°. The thick lines show the results for $\alpha = 10°$.

two-dimensional inviscid flow, and the swirl velocity by Γ_0/c. The velocity profiles are similar for all angles of attack, with a maximum of order unity located at a radial distance $r_m \approx 0.05c$, which defines the core radius. The rescaled circulation profiles are identical up to about twice the core radius (shaded region in Fig. 5b and circle in Fig. 4b). For an untwisted rectangular airfoil in inviscid flow, the spanwise distribution of non-dimensional bound circulation, as well as the radial circulation distribution of the resulting tip vortex which can be deduced from it [49], depend only on the aspect ratio [50]. The total circulation for $B/c = 5.8$ is predicted as $0.82\,\Gamma_0$. The fact that the profiles in Fig. 5(b) depend also on the angle of attack is due to the non-linearity of the lift curve of the NACA 0012 airfoil for $Re = 10^5$. Theoretical calculations using a lift curve based on recent experimental results [51, 52] predict total circulations between $0.94\,\Gamma_0$ (for $\alpha = 4°$) and $0.68\,\Gamma_0$ (for $\alpha = 12°$), and reproduce well the profiles measured in the present study.

3.2. Effect of a tip fin placed on the suction or pressure side

The desired secondary vortex is generated by means of the additional fin placed on either the suction or the pressure side of the wing. It is expected that the fin has a significant impact on the flow behaviour close to the wingtip due to the three-dimensional flow characteristics in this region. Oil flow visualisations provide an insight into the flow near the wing surface, an example is given in Fig. 6. The wing is mounted vertically on an adjustable rotating plate, with gravity directed towards the wing root. Both suction and pressure sides are shown for the reference case without fin (Fig. 6a,b) and a modified configuration with fin (Fig. 6c,d). The flow pattern for the reference case in Fig. 6(a) indicates the presence of a small separation bubble on the suction side close to the leading edge for the investigated flow conditions. The cross flow caused by the pressure difference between the two wing surfaces, and the subsequent vortex formation process, can clearly be identified in the tip region of the bare wing. In comparison, the flow patterns of the modified wing reveal some remarkable effects related to the presence of the fin.

a) Bare wing, suction side | **b) Bare wing, pressure side** | **c) Modified wing, suction side** | **d) Modified wing, pressure side**

Fig. 6. Oil flow pattern for the reference case and a modified configuration at $Re = 100,000$ and $\alpha = 10°$. For a better comparison, the pressure sides are mirrored. Fin geometry for (c,d): $d/c = 0.5$, $h/c = 0.3$, $\alpha_f = 10°$, flow is from left to right.

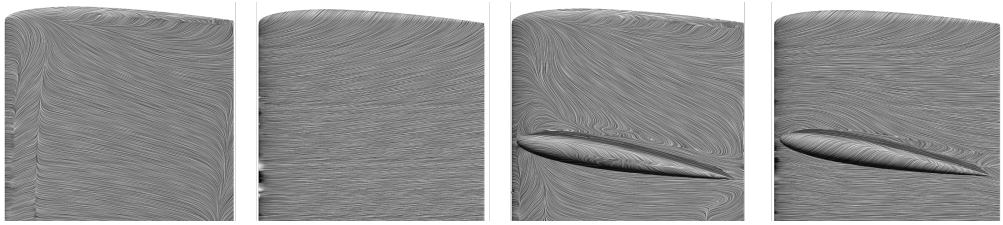

a) Bare wing, suction side | **b) Bare wing, pressure side** | **c) Modified wing, suction side** | **d) Modified wing, pressure side**

Fig. 7. Flow pattern obtained from simulation results, created by the LIC method, for the same cases as in Fig. 6.

The observed flow behaviour is very different when the fin is mounted either on the suction or the pressure side. In the former case (Fig. 6c), a large separation region above the fin's suction side is visible, similar to corner flow separation, inducing a recirculation region adjacent to the trailing edge of the wing. This phenomenon was also observed in preliminary visualisations in the water channel and was expected to have a negative impact on the vortex formation at the fin tip and possible mutual interactions downstream. A decrease of the fin angle down to $\alpha_f = 6°$ does not lead to a reattachment of the flow, giving the impression that the inflow conditions on the suction side are prone to corner flow separation, irrespective of the geometric specifications of the fin. Also, a variation of the spanwise position d yields no notable differences concerning the separation, implying that the influence of the cross flow in the tip region is not decisive for the detected effect. Potential explanations for this flow behaviour include interactions with the separation bubble close to the leading edge and a blocking effect of the main wing, causing non-uniform inflow conditions for the fin.

Several numerical simulations of selected configurations were performed to analyse in more detail the observations obtained from the oil painting visualisations. For comparison, an image equivalent to the oil painting pattern can be generated by the Line Integral Convolution (LIC) method. The result, displayed in Fig. 7 for the same configurations as in Fig. 6, shows good agreement with the experimental observations. The differences between simulation and experiment concerning the flow patterns close to the trailing edge of the wing can be explained by the

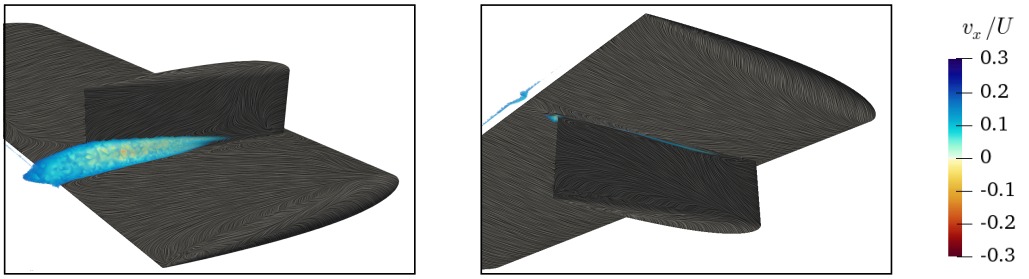

a) Suction side **b) Pressure side**

Fig. 8. Illustration of the separation tendency close to the fin root at an angle of attack of $\alpha = 10°$ for a fin position on (a) the suction and (b) the pressure side of the main wing. Fin geometry: $d/c = 0.5$, $h/c = 0.3$, $\alpha_f = 10°$.

influence of gravity on the oil film; resulting from the wing positioning in the wind tunnel.

Fig. 8 shows isosurfaces of the streamwise velocity v_x, in order to illustrate the size of the separation regions for both fin configurations (for visual clarity, the isosurfaces within the prism layers of the numerical mesh are not displayed). With the fin placed on the suction side (Fig. 8a), a significant flow separation region appears close to the fin root, even at moderate angles of attack. Although the numerical results show that, despite the presence of partly separated flow regions, a secondary vortex is generated at the fin tip (see below), an influence of the separation on the fin vortex formation, which might cause undesired perturbations prior to possible interactions with the wingtip vortex, cannot be ruled out.

The experimental and numerical results indicate that the impact on the surrounding flow field of a fin mounted on the pressure side of the wing is notably smaller. The flow pattern obtained by oil painting (Fig. 6d) shows no evidence of flow separation, similar to the LIC pattern in Fig. 7(d). Contrary to the suction side, the flow around the fin is well attached over the entire wingspan, providing favourable conditions for the formation of a secondary vortex. These impressions from the flow pattern are supported by the numerical results in Fig. 8(b) which show no evidence of separation regions close to the fin. The generation of the primary wing vortex appears not to be influenced by the presence of the fin or the secondary vortex.

Based on these findings it was decided that further SPIV investigations in this study should focus on configurations with the fin mounted on the pressure side of the wing. For this arrangement, a positive fin angle α_f (see Fig. 1) results in a co-rotating vortex system, whereas negative fin angles produce a counter-rotating secondary vortex. Considering the effects of the cross flow on the lower surface close to the wingtip, a slight deflection of the free stream approaching the fin occurs, causing a de- or increase of the effective angle of attack, depending on the fin orientation. A numerical parameter study, including a variation of α_f for constant $d/c = 0.3$ and $h/c = 0.3$, was performed to investigate this hypothesis. For all configurations, a constant angle of attack $\alpha = 10°$ was chosen.

The result is shown in Fig. 9. Several cuts along the chord display the normalised streamwise vorticity ω to qualitatively illustrate the vortex generation process. The parameter variation reveals that the neutral position of the fin, indicated by the absence of a secondary fin vortex, is located between $\alpha_f = -4°$ and $\alpha_f = -6°$ for the chosen fin configuration. It is expected that the influence of the cross flow decreases for greater values of the fin distance d. As a consequence of this asymmetry in the fin vortex formation, with respect to the fin angle value, it is expected that

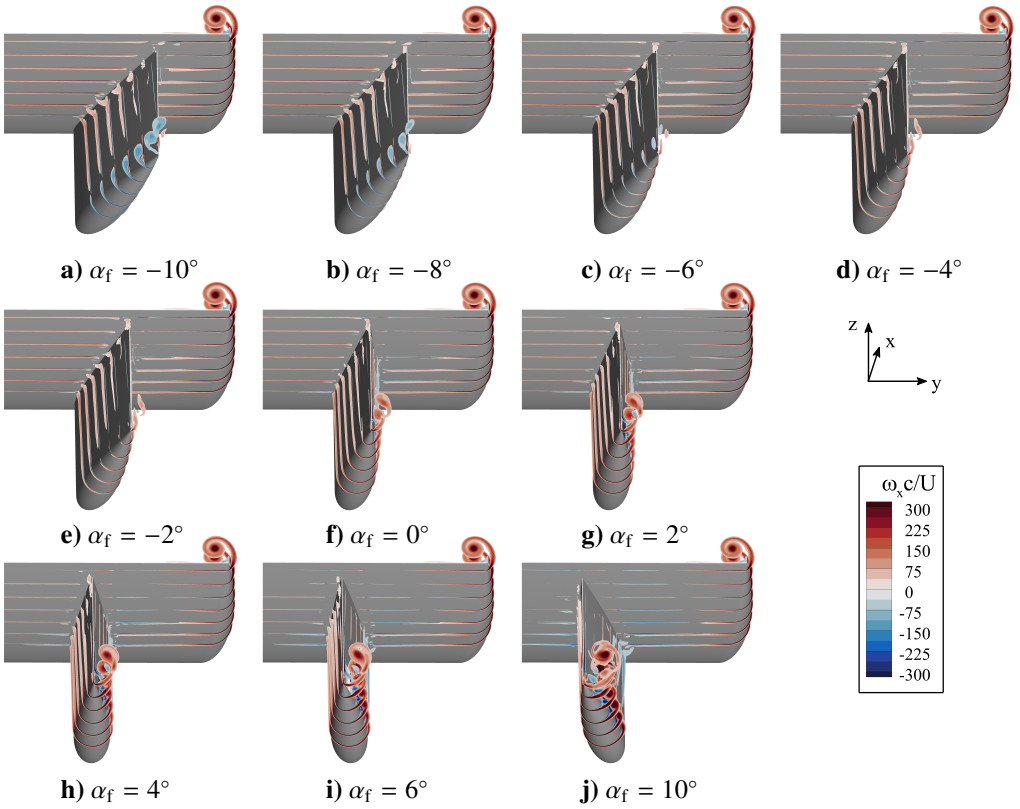

Fig. 9. Vortex formation at the fin and wingtips for different fin angles, illustrating the effect of the cross flow close to the wingtip. The neutral position (no fin vortex) is shifted to $\alpha_f \approx -5°$. $d/c = 0.3$ and $h/c = 0.3$ for all cases.

counter-rotating fin vortices are weaker than co-rotating ones, for the same absolute values of the fin angle. If strong interactions with the wingtip vortex are likely to occur when the fin vortex has a comparable strength, the co-rotating configurations, with positive α_f, therefore appear more promising.

3.3. Co- and counter-rotating tip vortex pairs

The experimental investigation of the effect of the fin is again carried out using SPIV measurements in the near wake of the wing. In this section, two representative configurations are analysed in detail. In the first, the wing/fin geometry generates a co-rotating pair of vortices of approximately the same circulation, which is expected to be favorable for the development of vortex interactions and instabilities, as well as merging. The second fin configuration creates a counter-rotating secondary vortex, whose strength is significantly lower than the one of the wingtip vortex, for the reasons discussed above. Figures 10 and 11 present the distributions of streamwise vorticity for the two configurations, measured in different cross-sections of the flow downstream of the wing. The fields were obtained by averaging 350 instantaneous distributions. In both cases, the wing angle of attack is $\alpha = 10°$.

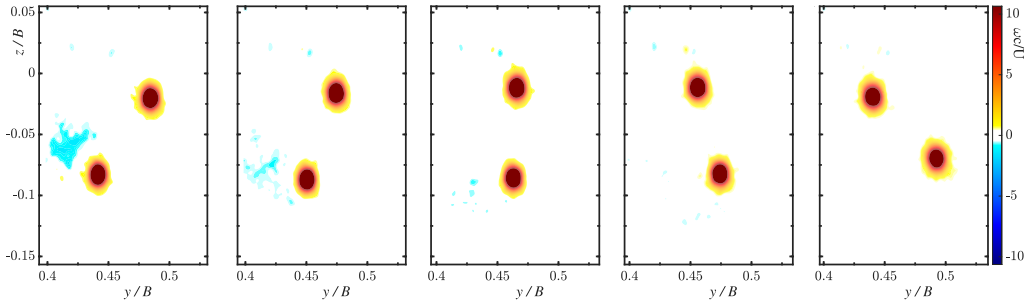

a) $x/c = 1$ **b)** $x/c = 2$ **c)** $x/c = 3$ **d)** $x/c = 4$ **e)** $x/c = 6$

Fig. 10. Vorticity fields in different planes behind the wing, illustrating the development of a co-rotating vortex system. The fin parameters are: $d/c = 0.3$, $h/c = 0.3$, $\alpha_f = 10°$.

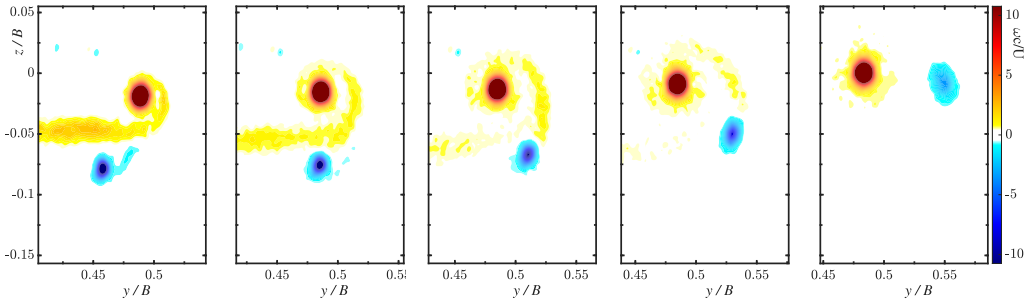

a) $x/c = 1$ **b)** $x/c = 2$ **c)** $x/c = 3$ **d)** $x/c = 4$ **e)** $x/c = 6$

Fig. 11. Vorticity fields illustrating the evolution of a counter-rotating vortex system. The fin parameters are: $d/c = 0.5$, $h/c = 0.3$, $\alpha_f = -12°$.

The co-rotating vortex system is generated by a wing equipped with a fin located on the pressure side at a distance $d/c = 0.3$ from the tip, and having a height $h/c = 0.3$ and angle of attack $\alpha_f = 10°$. Figure 10 reveals that at one chord length behind the trailing edge of the wing ($x/c = 1$) two concentrated vortices have formed from the wingtip (upper vortex) and fin tip (lower vortex). Both vortices exhibit a stable core structure, and they rotate around each other while propagating downstream, as expected for the co-rotating configuration.

The averaged SPIV velocity fields can again be used to determine the vortex characteristics (radius, circulation), with the procedure described in section 3.1 (Fig. 5). The evolution of the core radii is shown in Fig. 12. For a better comparison with theoretical results, the equivalent Gaussian core size $a = r_m/1.12$ is displayed. The initial radius of the wingtip vortex is practically unchanged by the presence of the fin. The fin vortex has a comparable, slightly smaller size. The downstream evolution of the core radii shows good agreement with the theoretical predictions for two-dimensional viscous Gaussian vortices of similar initial size, which can be deduced from the temporal evolution based on the diffusion of vorticity: $a^2(t) = a^2(t = 0) + 4\nu t$. The latter are shown as dashed lines in Fig. 12. The apparent laminar viscous growth of the vortex cores suggests the absence of interaction and instability phenomena at this early stage, which would typically lead to a faster core growth. In the observation interval ($x/c \leq 6$), the rescaled core radius a/b, where b is the distance between vortex centres, remains well below the critical value

of $a/b = 0.24$ for the onset of merging [9], so that the formation of a single vortex through this process is only expected much further downstream.

The circulation values for the co-rotating vortex system are plotted in Fig. 13. They were obtained by integrating the streamwise vorticity in a circular area of radius $0.15c$ around the given vortex centre. The same radius was also used for all other circulation measurements shown in the following, to allow for a better comparison. It is large enough to capture the core vorticity, and at the same time small enough not to include circulation from the low-intensity vorticity sheet shed behind the wing, nor circulation that may be attributed to the other vortex of the pair, i.e. it is less than $b/2$ for all cases considered. For the chosen co-rotating configuration, the wingtip and and fin vortex circulations are almost identical, and they vary little in the observation interval. It should be noted that the total circulation of the two vortices is about 20% larger than the circulation of the tip vortex without fin and otherwise identical wing parameters.

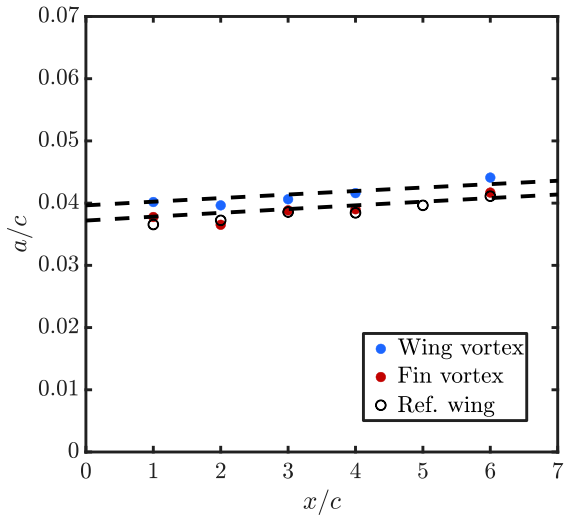

Fig. 12. Vortex core radii for the co-rotating system. The dashed lines show the expected viscous evolution for a laminar Gaussian vortex.

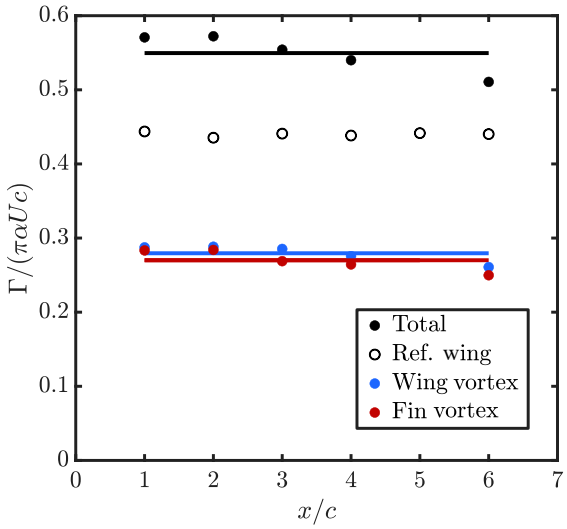

Fig. 13. Vortex circulations in the co-rotating system.

Thus it appears that the additional fin does not only split up the single vortex, but also influences the amount of bound circulation (see also Fig.16), and therefore the lift and induced drag characteristics of the wing.

The geometric fin parameters for the counter-rotating vortex pair case shown in Fig. 11 are $d/c = 0.5$, $h/c = 0.3$ and $\alpha_f = -12°$. Two vortices of opposite-signed vorticity are generated by this configuration. Despite the high fin angle, the (lower) secondary vortex is notably weaker than the (upper) tip vortex, in agreement with the results from the numerical simulations.

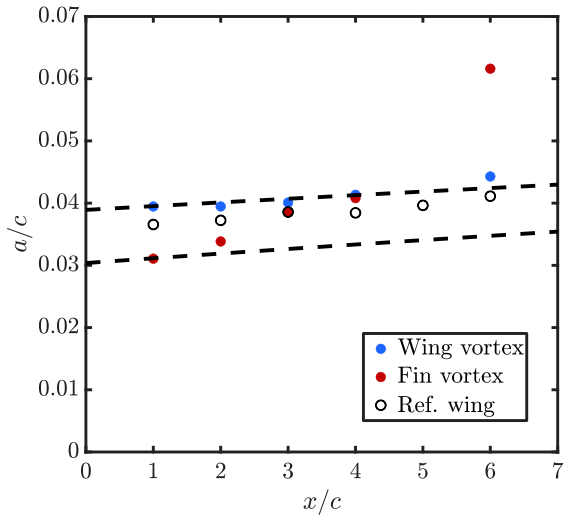

Fig. 14. Vortex core radii for the counter-rotating system. Dashed lines: viscous evolution.

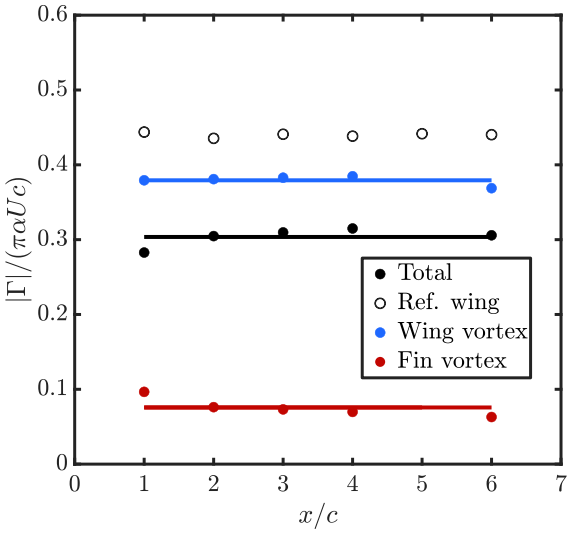

Fig. 15. Vortex circulations in the counter-rotating system.

Whereas the tip vortex core remains fairly unchanged up to $x/c = 6$, the core of the fin vortex is being stretched by the strain induced from the much stronger tip vortex. One can see in Fig. 11(e) that it starts getting wrapped around the latter, suggesting that it is likely to get ripped apart later on. This process is reflected in the evolution of the core size in Fig. 14. Contrary to the tip vortex, which again evolves approximately like a two-dimensional laminar vortex, the radius of the fin vortex increases much faster. The measurements of the circulation in Fig. 15 confirm that the strength of the fin vortex is only about 20% of the one of the wingtip vortex. Compared to the reference case, the total circulation is significantly diminished by the addition of the fin.

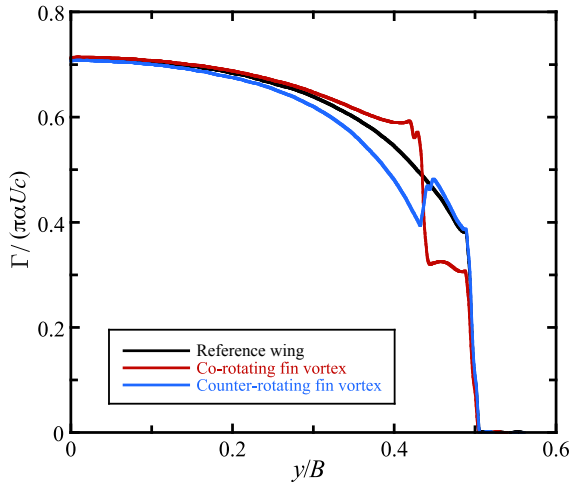

Fig. 16. Spanwise circulation distribution for the co- and counter-rotating cases shown in Figs. 10 and 11, compared to the reference wing without fin.

Figure 16 displays the spanwise distributions of the normalised circulation for the two fin configurations, as well as for the reference wing without fin. They were deduced from the spanwise vorticity field immediately downstream of the trailing edge of the wing, obtained by numerical simulation. The result obtained for the reference wing is in good agreement with the Prandtl model for a finite-span rectangular wing [50], the small deviation (kink) in the tip region can be explained by the incipient roll-up of the tip vortex. The circulation profiles of the modified configurations reflect well the presence of the additional secondary vortices. They manifest themselves through an additional sharp decrease or increase of the radial distribution, their amount corresponding to the circulations seen in Figs.13 and 15. Further away from the tip region (for $y/B < 0.3$), the circulation distributions for all cases converge.

For both co- and counter-rotating systems, the influence of the additional fin on the generated lift or drag has not been analysed experimentally within the scope of this work. The circulation distributions obtained from the numerical simulations in Fig. 16 reveal that the fin has an effect on the bound circulation which is directly related to the lift distribution. In addition, the drag characteristics of the wing are likely to be affected by the presence of the fin as well. A more detailed analysis of the effect of the fin on the aerodynamic performance of the wing is planned for future work.

3.4. Parameter study

The geometry and position of the fin which generates the secondary tip vortex are determined by the parameters shown in Fig.1. We now discuss how the variation of these parameters influences the characteristics of the resulting vortex pair, using the results from a series of SPIV measurements. For this analysis, the following parameter values were considered: wing angle $\alpha = 6°, 10°$; fin angle $\alpha_f = \pm 6°, \pm 10°$; fin height $h/c = 0.3, 0.5$; fin position $d/c = 0.2, 0.3, 0.5$. The tip vortex pair is characterised by the circulation (Γ) and core size (a) of each vortex, as well as the distance between the vortex centres (b).

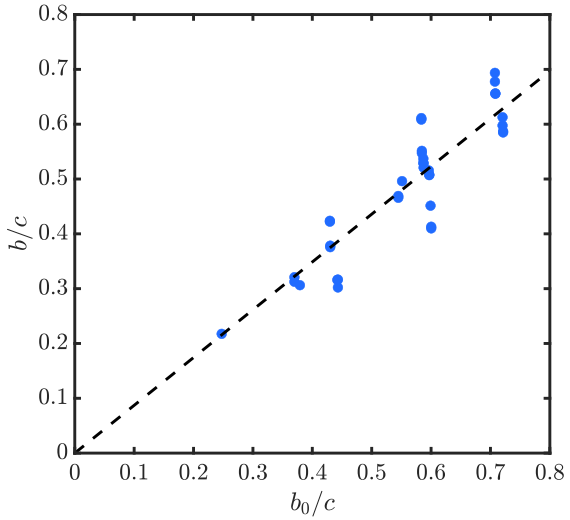

Fig. 17. Vortex separation b, measured at $x/c = 1$, as function of the geometrical distance b_0 between wing and fin trailing edge tips, for all tested configurations.

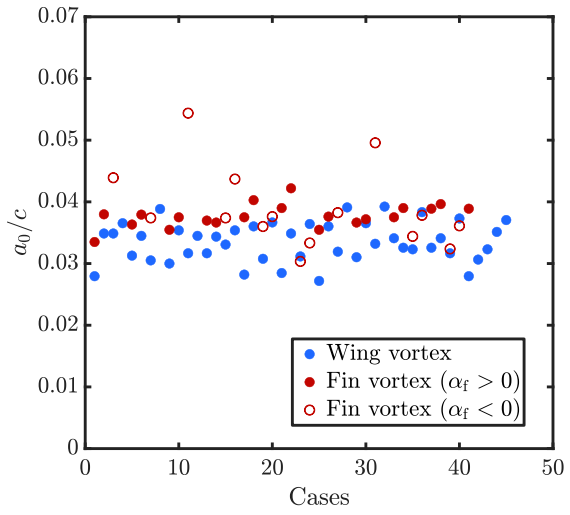

Fig. 18. Gaussian core radius a for all configurations.

The initial vortex separation is determined by the wingtip/fin geometry; it was found to be close to the distance b_0 between the tips of the trailing edges of the wing and the fin, as illustrated in Fig. 17. The initial core radii of the wing and fin tip vortices depend mainly on the respective chord lengths, which were not varied in this study. For all tested co-rotating configurations, they were found to lie in the range $0.03 \leq a/c \leq 0.04$ (see Fig. 18). The configurations equipped with fins having negative angles α_f generate fin vortices significantly weaker than the corresponding wing vortices, compare Fig. 15. Hence their geometry is stretched and deformed by the presence wing vortex immediately after emerging from the trailing edges, explaining the outliers in Fig. 18.

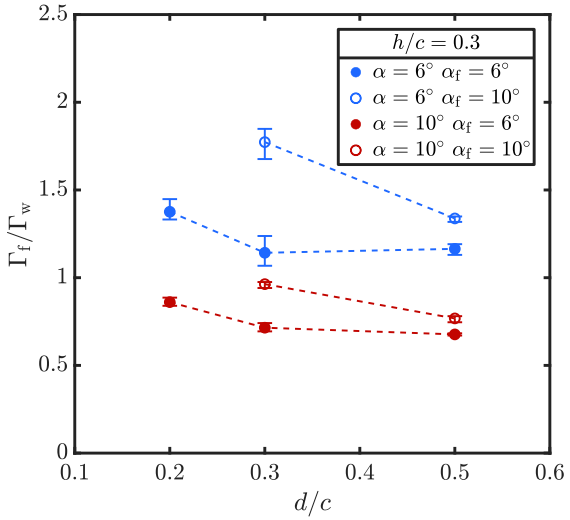

Fig. 19. Variation of the circulation ratio with fin position, for various combinations of angles of attack. The fin height is $h/c = 0.3$ for all cases.

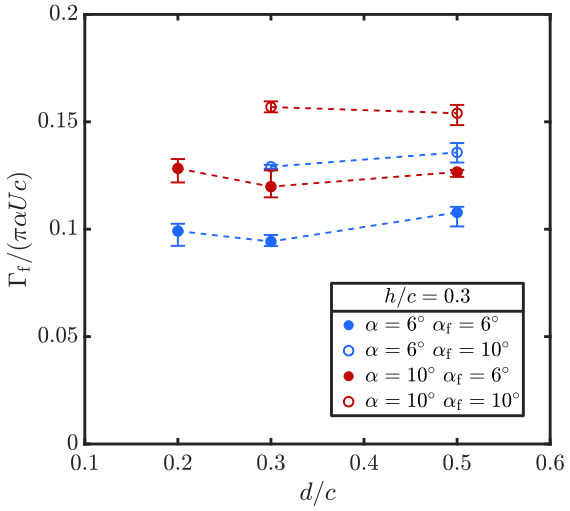

Fig. 20. Variation of the fin vortex circulation with fin position, for various combinations of angles of attack. $h/c = 0.3$.

The remainder of this section focusses on circulations Γ_w (wingtip vortex) and Γ_f (fin vortex), and their ratio, whose variation as function of the geometric parameters is less straightforward. We consider mostly co-rotating configurations, since these are more relevant for possible applications in aeronautics. In these cases, maximum spreading of the vorticity is obtained for circulation ratios Γ_f/Γ_w close to 1. In the following, a single circulation value is used for each vortex of a given configuration. It is determined by averaging the measurements made in the near wake of the wing up to $x/c = 6$, as shown e.g. in Figs. 13 and 15.

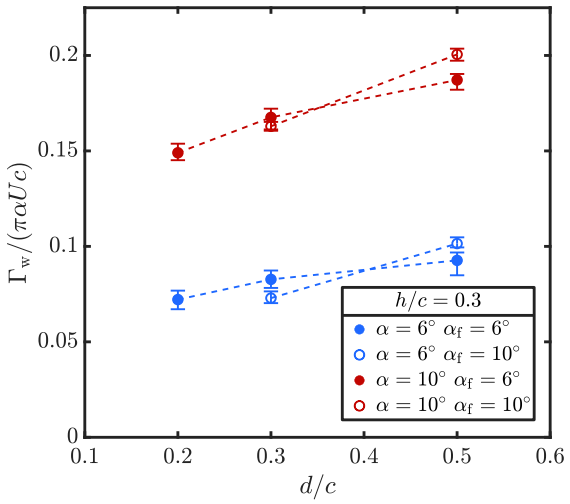

Fig. 21. Variation of the wingtip vortex circulation with fin position, for various combinations of angles of attack. $h/c = 0.3$.

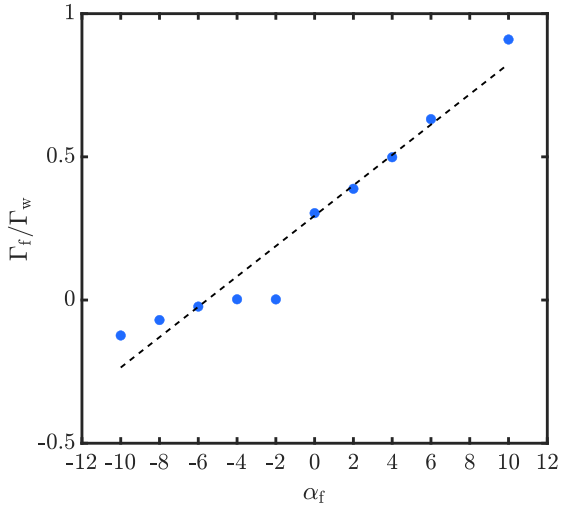

Fig. 22. Circulation ratio immediately behind the wing trailing edge as function of the fin angle. Data obtained from numerical simulations for $\alpha = 10^\circ$, $d/c = 0.3$ and $h/c = 0.3$ (see also Fig. 9).

Error bars indicate the minimum and maximum values found in this interval. Figure 19 shows the experimentally determined circulation ratios as function of the fin position, for four combinations of wing and fin angles. A slight decrease of the ratio is found in all cases, as the distance to the wingtip increases. As expected, the highest values (approaching $\Gamma_f/\Gamma_w = 2$) are found for low wing angle and high fin angle. The strength of the fin vortex alone depends little on the fin position, but exhibits a non-trivial variation with the angle-of-attack combinations (Fig. 20). It increases with the fin angle, but also by increasing only the angle of the main wing.

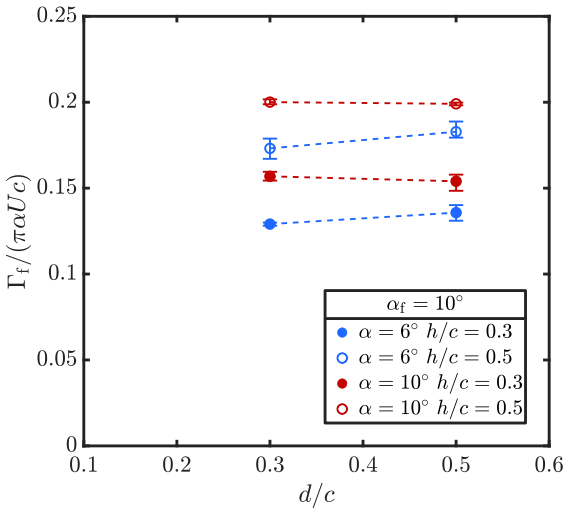

Fig. 23. Effect of fin height on the fin vortex circulation in co-rotating systems. The fin angle is constant (α_f = 10°).

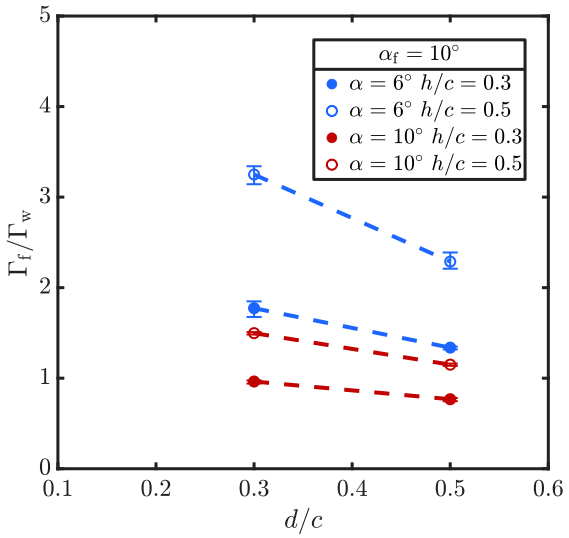

Fig. 24. Effect of fin height on the circulation ratio of co-rotating systems. α_f = 10°.

The circulation of the tip vortex is roughly proportional to the wing's angle of attack, as expected (Fig. 21), but its value is also significantly influenced by the position of the fin: it increases as the fin moves further away from the tip. These results show that the tip and fin vortices have a mutual influence on each other, and that their strength is not determined independently by the characteristics of the respective wingtip and fin geometries.

The previous results suggest that is it possible to control the circulation ratio Γ_f/Γ_w by adjusting the fin angle α_f, when the fin is placed near the wingtip. Figure 22 displays the relation

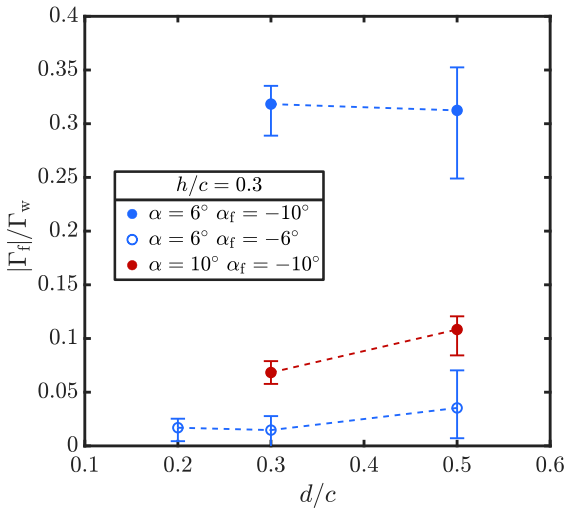

Fig. 25. Effect of fin position on the circulation ratio of counter-rotating systems. The fin height is constant ($h/c = 0.3$).

between both quantities, as determined from the numerical simulations, using the set of configurations shown in Fig. 9. The circulations are here determined in a plane immediately behind the wing trailing edge. For positive angles, the dependency is approximately linear, resulting from the increase of the fin vortex circulation with fin angle (Fig. 20) and the almost unchanged circulation of the wingtip vortex (Fig. 21). Negative fin angles exhibit a different behaviour, with the generated fin vortices being much weaker in comparison. The circulation ratio (absolute value) remains small and increases slightly only at large negative fin angles. As discussed in section 3.2, this asymmetry can probably be linked to the three-dimensionality of the flow in the wingtip region, which modifies the effective angle of attack of the fin. Overall, the result in Fig. 22 confirms the qualitative impressions from Fig. 9.

An increase of the fin height h/c has several effects. It makes the fin geometry less three-dimensional and moves the fin tip further away from the wing surface into the free stream. This is expected to lead to an increase of the fin vortex circulation, which is confirmed by the measurements shown in Fig. 23. At the same time, a larger fin further prevents the spanwise cross flow near the main wing surface and therefore disturbs the formation of the tip vortex. Both tendencies lead to a significant increase of the circulation ratio with h/c, as shown in Fig. 24. The effect is enhanced when the fin moves closer to the wingtip. For the configuration with $\alpha = 6°$, $\alpha_f = 10°$ and $h/c = 0.5$, a circulation ratio larger than 3 is found with the fin located at $d/c = 0.3$.

A smaller set of counter-rotating configurations with different parameter values was also investigated. As already noted in Fig. 22, the (absolute) circulation ratios are generally significantly smaller. In addition, Fig. 25 shows that there is a tendency for the ratio to increase as the fin moves away from the wingtip, which can be related to the diminishing influence of the tip vortex on the flow near the fin for increasing d/c. The effects on the circulation ratio of a variation of the fin height or of the wing angle of attack were found to be qualitatively similar to the ones observed for co-rotating configurations.

4. Conclusion

Through a combined experimental and numerical study, we have analysed the influence of a perpendicular fin, mounted close to the tip of a rectangular wing, on the generation of the trailing vortex system. This work was motivated by certain rotor blade tip geometries investigated in the past, aimed at splitting the concentrated tip vortex into two distinct vortices, which then undergo a mutual interaction and merging process resulting in a modified final vortex with altered characteristics (core radius, maximum swirl velocity). In the present study, a particular concept of generating two distinct tip vortices is explored for a fixed wing, in order to understand the fundamental mechanisms involved. The vortex splitting is achieved by adding a fin on the wing surface. When the fin is placed on the suction side of the wing, the experimental and numerical visualisations of the near-wall flow reveal a strong tendency for flow separation, which is detrimental to the formation of the secondary fin vortex. Most of the study therefore focussed on configurations with the fin on the pressure side, where no separation occurs. By adjusting the geometrical parameters defining the fin, it was possible to generate a variety of co- and counter-rotating vortex systems. These were characterised by the respective vortex circulations and radii, and the separation distance. The three-dimensional characteristics of the flow near the wingtip affects the performance of the fin. The cross flow on the wing surface in this region modifies the effective fin angle, which favours the generation of co-rotating vortices. An extensive parameter study has shown that it is possible to generate vortex systems with circulation ratios close to unity, resulting in an efficient spreading of the tip vortex vorticity. In addition, such pairs of nearly equal circulation are prone to develop strong mutual interactions and merge into a less concentrated final vortex, leading to less severe interactions with other structures (e.g. blade-vortex interactions generating noise in the case of a rotor). In the current investigation using a fixed-wing geometry, instabilities and merging of the tip and fin vortices were not observed in the near-wake region considered. In a related study [53–55] involving a rotating wing equipped with a similar fin, designed using the results presented here, a strong three-dimensional short-wave instability, followed by a rapid merging, was found. This interesting new behaviour appears to be related to the difference in the spanwise circulation distributions between fixed and rotating wings. It suggests that the wing tip modification using a fin may hold promise for reducing the level of undesired blade-vortex interactions in rotor flows.

Declaration of competing interest

There are no conflicts of interest to declare.

Acknowledgements

This work is part of the German-French project TWIN-HELIX, supported by the *Deutsche Forschungsgemeinschaft* (grant no. 391677260) and the French *Agence Nationale de la Recherche* (grant no. ANR-17-CE06-0018).

References

[1] H. Schlichting, E. A. Truckenbrodt, Aerodynamik des Flugzeuges. Zweiter Band, 3rd Edition, Springer, Berlin, 2001.

[2] V. J. Rossow, Lift-generated vortex wakes of subsonic transport aircraft, Prog. Aerosp. Sci. 35 (1999) 507–660. doi:10.1016/S0376-0421(99)00006-8.

[3] T. Gerz, F. Holzäpfel, D. Darracq, Commercial aircraft wake vortices, Prog. Aerosp. Sci. 38 (2002) 181–208. doi:10.1016/S0376-0421(02)00004-0.

[4] C. Breitsamter, Wake vortex characteristics of transport aircraft, Prog. Aerosp. Sci. 47 (2011) 89–134. doi:10.1016/j.paerosci.2010.09.002.

[5] E. Coustols, E. Stumpf, L. Jacquin, F. Moens, H. Vollmers, T. Gerz, Minimised wake: a collaborative research programme on aircraft wake vortices, in: 41st AIAA Aerosp. Sci. Meet. Exhib., Reno, Nevada, USA, 2003. doi:10.2514/6.2003-938.

[6] V. J. Rossow, Theoretical study of lift-generated vortex wakes designed to avoid rollup, AIAA J. 13 (1975) 476–484. doi:10.2514/3.49734.

[7] V. R. Corsiglia, V. J. Rossow, D. L. Ciffone, Experimental study of the effect of span loading on aircraft wakes, J. Aircr. 13 (1976) 968–973. doi:10.2514/3.58737.

[8] L. Jacquin, D. Fabre, D. Sipp, E. Coustols, Unsteadiness, instability and turbulence in trailing vortices, C. R. Physique 6 (2005) 399–414. doi:10.1016/j.crhy.2005.05.007.

[9] T. Leweke, S. Le Dizès, C. H. Williamson, Dynamics and instabilities of vortex pairs, Annu. Rev. Fluid Mech. 48 (2016) 507–541. doi:10.1146/annurev-fluid-122414-034558.

[10] J. D. Crouch, G. D. Miller, P. R. Spalart, Active-control system for breakup of airplane trailing vortices, AIAA J. 39 (2001) 2374–2381. doi:10.2514/2.1244.

[11] D. Greenblatt, S. Vey, O. C. Paschereit, R. Meyer, Flap vortex management using active Gurney flaps, AIAA J. 47 (2009) 2845–2856. doi:10.2514/1.41767.

[12] V. J. Rossow, Effect of wing fins on lift-generated wakes, J. Aircr. 15 (1978) 160–167. doi:10.2514/3.58335.

[13] E. Özger, I. Schell, D. Jacob, On the structure and attenuation of an aircraft wake, J. Aircr. 38 (2001) 878–887. doi:10.2514/2.2847.

[14] S. Widnall, Helicopter noise due to blade–vortex interaction, J. Acoust. Soc. Am. 50 (1971) 354–365. doi:10.1121/1.1912640.

[15] F. H. Schmitz, Y. H. Yu, Helicopter impulsive noise: Theoretical and experimental status, J. Sound Vib. 109 (1986) 361–422. doi:10.1016/S0022-460X(86)80378-9.

[16] J. C. Hardin, S. L. Lamkin, Concepts for reduction of blade/vortex interaction noise, J. Aircr. 24 (1987) 120–125. doi:10.2514/3.45428.

[17] Y. H. Yu, Rotor blade–vortex interaction noise, Progr. Aerosp. Sci. 36 (2000) 97–115. doi:10.1016/S0376-0421(99)00012-3.

[18] W. Johnson, Rotorcraft Aeromechanics, Cambridge University Press, Cambridge, 2013. doi:10.1017/CBO9781139235655.

[19] A. Brocklehurst, G. N. Barakos, A review of helicopter rotor blade tip shapes, Progr. Aerosp. Sci. 56 (2013) 35–74. doi:10.1016/j.paerosci.2012.06.003.

[20] K. S. Brentner, F. Farassat, Modeling aerodynamically generated sound of helicopter rotors, Progr. Aerosp. Sci. 39 (2003) 83–120. doi:10.1016/S0376-0421(02)00068-4.

[21] A. Brocklehurst, A. C. Pike, Reduction of BVI noise using a vane tip, in: AHS Aeromech. Specialists Conf., San Francisco, California, USA, 1994.

[22] T. Leweke, H. U. Quaranta, H. Bolnot, F. J. Blanco-Rodríguez, S. Le Dizès, Long- and short-wave instabilities in helical vortices, J. Phys. Conf. Ser. 524 (2014) 012154. doi:10.1088/1742-6596/524/1/012154.

[23] V. L. Okulov, On the stability of multiple helical vortices, J. Fluid Mech. 521 (2004) 319–342. doi:10.1017/S0022112004001934.

[24] H. U. Quaranta, H. Bolnot, T. Leweke, Long-wave instability of a helical vortex, J. Fluid Mech. 780 (2015) 687–716. doi:10.1017/jfm.2015.479.

[25] H. U. Quaranta, M. Brynjell-Rahkola, T. Leweke, D. S. Henningson, Local and global pairing instabilities of two interlaced helical vortices, J. Fluid Mech. 863 (2019) 927–955. doi:10.1017/jfm.2018.904.

[26] D. W. Moore, P. G. Saffman, The instability of a straight vortex filament in a strain field, Proc. R. Soc. A 346 (1975) 413–425. doi:10.1098/rspa.1975.0183.

[27] R. R. Kerswell, Elliptical instability, Annu. Rev. Fluid Mech. 34 (2002) 83–113. doi:10.1146/annurev.fluid.34.081701.171829.

[28] F. J. Blanco-Rodríguez, S. Le Dizès, Elliptic instability of a curved batchelor vortex, J. Fluid Mech. 804 (2016) 224–247. doi:10.1017/jfm.2016.533.

[29] Y. Fukumoto, T. Miyazaki, Three-dimensional distortions of a vortex filament with axial velocity, J. Fluid Mech. 222 (1991) 369–416. doi:10.1017/S0022112091001143.
[30] Y. Hattori, Y. Fukumoto, Short-wave stability of a helical vortex tube: the effect of torsion on the curvature instability, Theor. Comput. Fluid Dyn. 24 (2010) 363–368. doi:10.1007/s00162-009-0145-2.
[31] Y. Hattori, Y. Fukumoto, Modal stability analysis of a helical vortex tube with axial flow, J. Fluid Mech. 738 (2014) 222–249. doi:10.1017/jfm.2013.591.
[32] R. Buffo, C. Wolf, S. Dufhaus, R. Hörnschemeyer, E. Stumpf, Vortex creation and wing-tip geometry dependencies, in: 30th AIAA Appl. Aerodyn. Conf., New Orleans, Louisiana, USA, 2012. doi:10.2514/6.2012-2770.
[33] N. J. Lawson, J. Wu, Three-dimensional particle image velocimetry: experimental error analysis of a digital angular stereoscopic system, Meas. Sci. Technol. 8 (1997) 1455–1464. doi:10.1088/0957-0233/8/12/009.
[34] A. K. Prasad, K. Jensen, Scheimpflug stereocamera for particle image velocimetry in liquid flows, Appl. Opt. 34 (1995) 7092–7099. doi:10.1364/AO.34.007092.
[35] M. Raffel, C. E. Willert, F. Scarano, C. J. Kähler, S. T. Wereley, J. Kompenhans, Particle Image Velocimetry: A Practical Guide, 3rd Edition, Springer International Publishing, Cham, 2018. doi:10.1007/978-3-319-68852-7.
[36] van der Wall, Berend G., H. Richard, Analysis methodology for 3c-piv data of rotary wing vortices, Experiments in Fluids 40 (2006) 798–812. doi:10.1007/s00348-006-0117-x.
URL https://doi.org/10.1007/s00348-006-0117-x
[37] W. J. Devenport, M. C. Rife, S. I. Liapis, G. J. Follin, The structure and development of a wing-tip vortex, J. Fluid Mech. 312 (1996) 67–106. doi:10.1017/S0022112096001929.
[38] D. Schwamborn, T. Gerhold, R. Heinrich, The DLR TAU-code: recent applications in research and industry, in: ECCOMAS CFD 2006 Conference, Egmond aan Zee, Netherlands, 2006.
[39] S. Langer, Investigation and application of point implicit Runge-Kutta methods to inviscid flow problems, Int. J. Numer. Methods Fluids 69 (2012) 332–352. doi:10.1002/fld.2561.
[40] B. Eisfeld, O. Brodersen, Advanced turbulence modelling and stress analysis for the DLR-F6 configuration, in: 23rd AIAA Appl. Aerodyn. Conf., Toronto, Ontario, Canada, 2005. doi:10.2514/6.2005-4727.
[41] S. Braun, A. Uhl, B. Eisfeld, E. Stumpf, Numerical simulation of vortex roll-up processes using the SSG/LRR-ω model, in: A. Dillmann, G. Heller, E. Krämer, C. Wagner, C. Breitsamter (Eds.), New Results in Numerical and Experimental Fluid Mechanics X, Vol. 132 of Notes on Numerical Fluid Mechanics and Multidisciplinary Design, Springer International Publishing, Cham, 2016, pp. 481–491. doi:10.1007/978-3-319-27279-5_42.
[42] B. Eisfeld, V. Togiti, S. Braun, A. W. Stuermer, Reynolds-stress model computations of the NASA juncture flow experiment, in: AIAA SciTech 2020 Forum, Orlando, Florida, USA. doi:10.2514/6.2020-1306.
[43] J. Dacles-Mariani, D. Kwak, G. Zilliac, On numerical errors and turbulence modeling in tip vortex flow prediction, Int. J. Numer. Methods Fluids 30 (1999) 65–82. doi:10.1002/(SICI)1097-0363(19990515)30:1<65::AID-FLD839>3.0.CO;2-Y.
[44] J. S. Chow, G. G. Zilliac, P. Bradshaw, Mean and turbulence measurements in the near field of a wingtip vortex, AIAA J. 35 (1997) 1561–1567. doi:10.2514/2.1.
[45] M. Giuni, R. B. Green, Vortex formation on squared and rounded tip, Aerosp. Sci. Technol. 22 (2013) 191–199. doi:10.1016/j.ast.2013.03.004.
[46] L. Jiang, J. Cai, C. Liu, Large-eddy simulation of wing tip vortex in the near field, Int. J. Comput. Fluid Dyn. 22 (2008) 289–330. doi:10.1080/10618560801938883.
[47] J.-E. W. Lombard, D. Moxey, S. J. Sherwin, J. F. A. Hoessler, S. Dhandapani, M. J. Taylor, Implicit large-eddy simulation of a wingtip vortex, AIAA J. 54 (2016) 506–518. doi:10.2514/1.J054181.
[48] J. Jeong, F. Hussain, On the identification of a vortex, J. Fluid Mech. 285 (1995) 69–94. doi:10.1017/S0022112095000462.
[49] C. duP. Donaldson, R. S. Snedeker, R. D. Sullivan, Calculation of aircraft wake velocity profiles and comparison with experimental measurements, J. Aircr. 11 (1974) 547–555. doi:10.2514/3.60385.
[50] E. Trefftz, Prandtlsche Tragflächen- und Propellertheorie, Z. Angew. Math. Mech. 1 (1921) 206–218. doi:10.1002/zamm.19210010307.
[51] T. Ohtake, Y. Nakae, T. Motohashi, Nonlinearity of the aerodynamic characteristics of NACA0012 aerofoil at low Reynolds numbers, J. Jpn Soc. Aeronaut. Space Sci. 55 (2007) 439–445. doi:10.2322/jjsass.55.439.
[52] J. Tank, L. Smith, G. R. Spedding, On the possibility (or lack thereof) of agreement between experiment and computation of flows over wings at moderate Reynolds number, Interface Focus 7 (2017) 20160076. doi:10.1098/rsfs.2016.0076.
[53] D. Schröder, T. Leweke, R. Hörnschemeyer, E. Stumpf, Experiments on helical vortex pairs in the wake of a rotor, in: AIAA SciTech Forum, 2021, Paper 2021-1088. doi:10.2514/6.2021-1088.
[54] D. Schröder, J. Aguilar-Cabello, T. Leweke, R. Hörnschemeyer, E. Stumpf, Experimental investigation of a rotor blade tip vortex pair, CEAS Aeronaut. J. (2021). doi:10.1007/s13272-021-00555-1.
[55] D. Schröder, T. Leweke, R. Hörnschemeyer, E. Stumpf, Instability and merging of a helical vortex pair in the wake of a rotor, J. Phys. Conf. Ser. 1934 (2021) 012007. doi:10.1088/1742-6596/1934/1/012007.